MAGNETOHYDRODYNAMICS Vol. 47 (2011), No. 1, pp. 17–28

# SIMULATIONS OF SILICON CZ GROWTH IN A CUSP MAGNETIC FIELD

*C.-H. Lin, P.-W. Chen, Ching-Yao Chen*†

*Department of Mechanical Engineering, National Chiao Tung University, Taiwan, Republic of China*

† *e-Mail: chingyao@mail.nctu.edu.tw*

This study numerically investigates the crystal growth subjected to a cusp direct current magnetic field. The numerical simulations, implemented by means of a commercial CGsim package, are based on the momentum equations coupled with energy transfer and electric current flow equations in the melt zone. Generally, the presence of the magnetic field stabilizes flow patterns of the melt, which is favorable to the processes of crystal growth. Detailed discussions regarding the flow fields and temperature distributions for the cases with various locations of the coils are presented. Determined by the overall factors, such as the interfacial shape and $V/G$ ratio, an intermediate distance of the coils' center above the melt interface is suggested for producing crystals of better quality.

**1. Introduction.** For a crystal, whose diameter is over 300 mm and even further over 450 mm in silicon (Si), grown by the Czochralski (CZ) method, the control of turbulently natural convection in large melt volumes is very important to engineers [1]. To improve the growth processes, different strengths with steady or unsteady magnetic fields, consisting of vertical (longitudinal), horizontal (transverse), cusp, and travelling fields in a combination with the other growth parameters can be applied. These effects lead to new characteristics of heat and mass transfer as well as to the convection phenomenon in the melt inside a crucible. For example, the melt flow becomes a nearly laminar flow if a sufficient field strength is applied [2]. In addition, the melt flow field becomes very smooth by applying a travelling magnetic field [3]. On the other hand, the melt flow becomes fully turbulent for the case of 300 mm crystal growth without magnetic effects [4]. Therefore, applying a magnetic field is an effective way to control the melt convection inside the crucible and obtain an optimal crystallization front and the $V/G$ distribution (where $V$ is the pulling rate, and $G$ is the axial temperature gradient in the crystal). However, the development of crystal growth experiments and magnet systems are costly, and the measurement of the melt and crystal interface is very difficult. In the last few decades, numerical simulation software has become a powerful tool to reduce experimental costs and provide physical understandings as well as quantitative predictions for industrial applications. Many detailed steady or unsteady models of the melt flows and heat transfers in the crystallization zone that use a variety of magnetic fields in the whole furnace have been presented to investigate the motion and energy transfer of the melt as well as the possible effects on the Si crystal growth [5–20]. Nevertheless, the effects of height variations for the magnet coils of a cusp field configuration on the melt flows and heat transfer profiles in the crucible for the Si CZ technique has not yet been thoroughly studied. Here, we investigate the melt flows and temperature fields in the crucible as well as the corresponding interface deflection and the $V/G$ parameter for Si CZ crystal growths by adjusting the locations of the magnet coils. The physical and mathematical formulation is illustrated first in Section 2. The numerical method

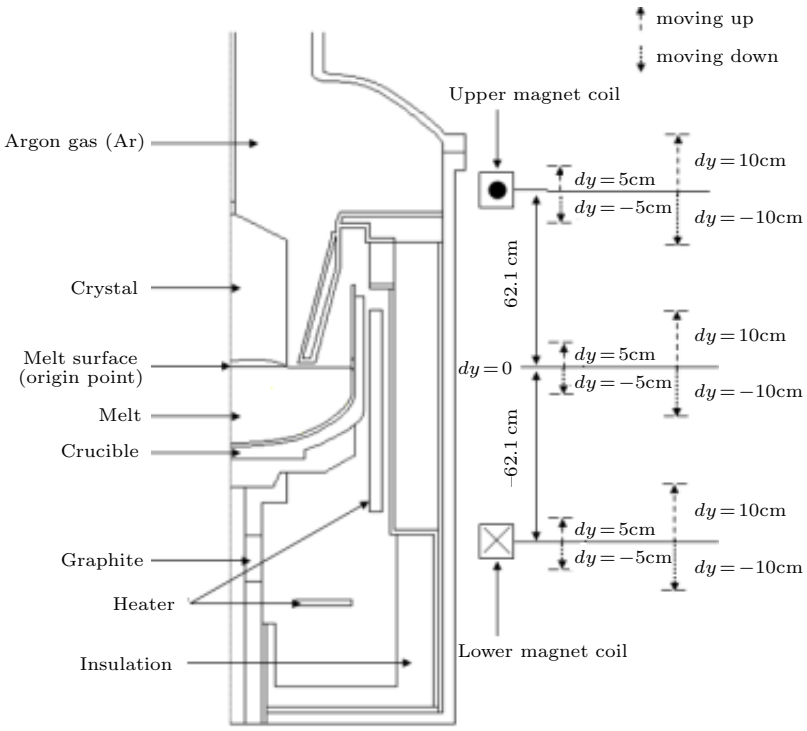


*Fig. 1.* Sketch of the 450 mm furnace and the positions of magnet coils.

and its validation are presented in Section 3. In Section 4, we discuss the effects of different magnet coils' locations on the melt flows and temperature distributions as well as the corresponding profiles of the crystallization front and the $V/G$ parameters.

**2. Physical model and mathematical formulation.**

*2.1. Physical model.* An axisymmetric schematic view of the furnace's cross-section is shown in Fig. 1. The diameter of the crucible, the crystal length, and the crystal diameter are 38 inches, 500 mm, and 450 mm, respectively. A cusp magnetic field is generated by the upper and lower magnet coils. The upper/lower magnet coils are spaced $\pm 62.1$ cm apart from their center. The center of the coils (or the horizontal zero-flux axis) is placed at a certain distance away from the melt surface denoted as $dy$. In this work, we vary the positions of the coils' locations from $dy = 5$ and 10 cm (above the melt surface) to $dy = -5$ and $-10$ cm (below the melt surface). We would like to point out that such a cusp field generates four close-loop magnetic fluxes in the four quadrants. The close-loop fluxes are clockwise in the first (right half part of the melt) and third quadrants, while they are counter-clockwise in the second and fourth (left half part of the melt) quadrants, respectively.

*2.2. Mathematical formulation.* The mathematical model used in this work consists of two parts. The first part is a global axisymmetric steady heat transfer in the whole growth system, including the inert gas flow, melt flow, and conductive heat transfer in solid blocks as shown in Fig. 2*a*. The second part is an axisymmetric steady Flow Module, which focuses on the local flow and heat transfer in the crystallization zone involving the crucible, silicon melt, crystal, and a limited gas region as demonstrated in Fig. 2*b*. The turbulence model is incorporated

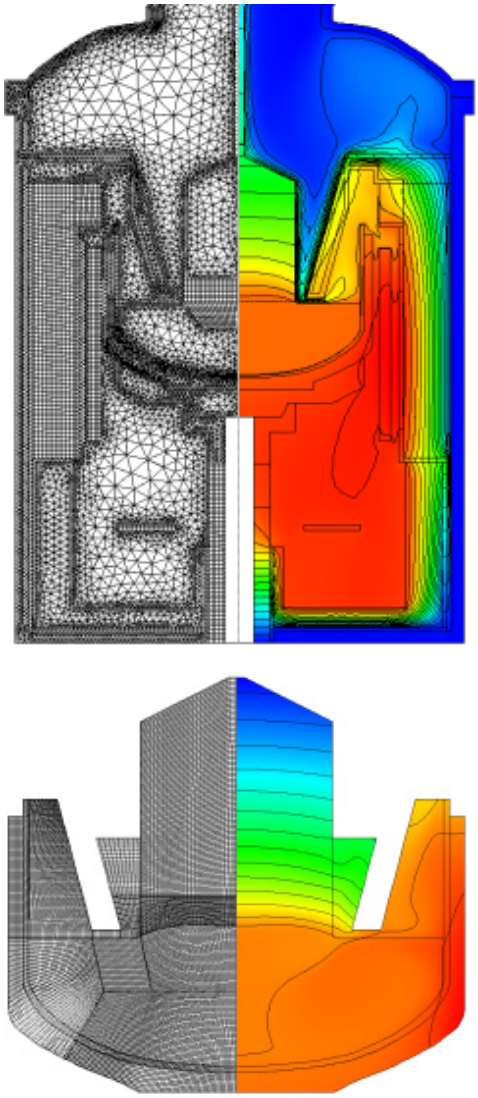

*Fig. 2.* (*a*) Grid structure (left) and simulated temperature distribution (right) for the global domain; (*b*) grid (left) and temperature (right) for the local Flow Module domain.

in the Flow Module. Four turbulence models, such as the one-equation model, a Spalart-Almaras model, the Chien $k$-$\epsilon$ model, and the standard $k$-$\epsilon$ model are tested and compared with the previous experimental results [21] to determine the appropriate turbulence model. The governing equations of continuity, momentum, heat transfer, and induced magnetic field can be written as

$$\nabla \cdot (\rho \, \mathbf{v}) = 0, \tag{1}$$

$$(\mathbf{u} \cdot \nabla) \, \rho \mathbf{u} = -\nabla p + \nabla \cdot \boldsymbol{\tau} + (\rho - \rho_0) \, \mathbf{g} + \mathbf{j} \times \mathbf{B}, \tag{2}$$

$$\nabla \cdot (\rho \, C_p \mathbf{u} T) = \nabla \cdot (\lambda_{\text{eff}} \nabla T) \, , \tag{3}$$

$$\Delta \Phi = \mathbf{B} \cdot (\nabla \times \mathbf{u}) \, , \tag{4}$$

Here, $\mathbf{u}$ is the velocity, $\mathbf{g}$ is the gravity vector, $C_p$ is the specific heat, $T$ is the temperature, $\mathbf{B}$ is the magnetic induction, and $\Phi$ is the electric potential. In addition, $\boldsymbol{\tau}$, $\rho$, $\lambda_{\text{eff}}$, and $\mathbf{j}$ are the stress tensor, the density, the effective thermal conductivity, and the electrical current, respectively, as shown by the following expressions:

$$\boldsymbol{\tau} = \mu_{\text{eff}} \left( \frac{\partial u_i}{\partial x_j} + \frac{\partial u_j}{\partial x_i} \right) - \frac{2}{3} \mu_{\text{eff}} \delta_{ij} \nabla \cdot \mathbf{u}, \tag{5}$$

$$\rho = \frac{p_0 m}{RT}, \tag{6}$$

$$\lambda_{\text{eff}} = \lambda + \frac{\mu_{\text{t}}}{\text{Pr}_{\text{t}}}, \tag{7}$$

$$\mathbf{j} = \sigma \left( -\nabla \Phi + \mathbf{u} \times \mathbf{B} \right). \tag{8}$$

Here, $\mu_{\text{eff}}$ is the effective dynamic viscosity (the sum of the laminar viscosity and the turbulent viscosity, i.e. $\mu_{\text{l}} + \mu_{\text{t}}$), $\delta_{ij}$ is the Kronecker delta, $p_0$ is the reference pressure, $m$ is the molecular weight, $R$ is the gas constant, $\text{Pr}_{\text{t}}$ is the turbulent Prandtl number, and $\sigma$ is the electrical conductivity.

The simulated conditions of crystal growth are taken as follows: the initial weight of the silicon charge is 650 kg. The mean crystallization rate is maintained at 0.5 mm/min. The crucible counter-rotating rate is –3 rpm and the crystal rotating rate is 5 rpm. The pressure of argon gas (Ar) is 0.024 bar and its flow rate is 355 slpm (standard liter per min). The boundary conditions along the melt free surface are determined by the momentum exchange between the melt and the gas as

$$\mathbf{u}_{\text{gas}} = \mathbf{u}_{\text{melt}}, \tag{9}$$

$$\mu \frac{\partial u_{\tau i}}{\partial n}\bigg|_{\text{gas}} = \mu_{\text{eff}} \frac{\partial u_{\tau i}}{\partial n}\bigg|_{\text{melt}} + \frac{\partial \Theta}{\partial T} \nabla_{\tau i} T. \tag{10}$$

Here, $\tau i$ is the orthogonal direction tangential to the free surface, and $\Theta$ is the liquid Si surface tension, respectively.

**3. Numerical method and validation.** The numerical schemes apply a finite volume technique with a third and a second order of accuracy for the convection and diffusion terms, respectively. A global heat transfer computation, such as shown in Fig. 2*a*, is performed to obtain relevant information within the whole system. Consequently, the information is applied as the boundary conditions for more detailed and accurate Flow Module simulations, whose domain and grid structure is demonstrated in Fig. 2*b*. The governing equations are solved again to achieve the desired results. The overall computational procedure is implemented by means of a commercial CGsim package (version 9.02) [22]. Physical properties used in the calculations are displayed in Table 1.

To verify the credibility of numerical results, a bench mark testing calculation is performed by taking identical physical conditions, whose crystal height and diameter are 300 and 100 mm, respectively, without influences of magnetic fields. Comparisons of the experimental data of the interface deflection value with the present numerical results for different turbulence models in the Flow Module are shown in Fig. 3. It is clear that the computational results by the Chien $k$-$\epsilon$ model approach most closely the experimental data. As a result, the Chien $k$-$\epsilon$ model is taken in the following calculations.

*Table 1.* Physical properties used in the simulations.

| Material | Variable | Value | Unit |
|---|---|---|---|
| Argon | Conductivity | $0.01 + 2.5 \times 10^{-5}T$ | W/m·K |
| | Heat capacity | 521 | J/kg.K |
| | Molar weight | 40 | kg/kgmol |
| | Dynamic viscosity | $8.46 \times 10^{-6} + 5.365 \times 10^{-8}T - 8.682 \times 10^{-12}T^2$ | Pa·s |
| | Emissivity | 0.8 | — |
| Graphite | Conductivity | Graphite function | W/m·K |
| | Emissivity | 0.8 | — |
| Quartz | Conductivity | 4 | W/m·K |
| | Density | 2650 | kg/m$^3$ |
| | Heat capacity | 1232 | J/kg·K |
| | Emissivity | 0.85 | — |
| Silicon crystal | Conductivity | $98.89 - 0.0943T - 2.89 \times 10^{-5}T^2$ | W/m.K |
| | Density | 2330 | kg/m$^3$ |
| | Heat capacity | 1000 | J/kg.K |
| | Emissivity | $0.9016 - 0.00026208T$ | — |
| Liquid silicon | Conductivity | $-2.001 + 0.0349T$ | W/m.K |
| | Dynamic viscosity | $8.225 \times 10^{-4}$ | Pa.s |
| | Heat capacity | 860 | J/kg.K |
| | Density | $3194 - 0.3701T$ | kg/m$^3$ |
| | Melting temperature | 1685 | K |
| | Latent heat | 1800000 | J/kg |
| | Surface tension | 0.7835 | N/m |
| | Wetting angle | 11 | deg |
| | Electric conductivity | $1.23 \times 10^6$ | S/m |
| | Emissivity | 0.3 | — |

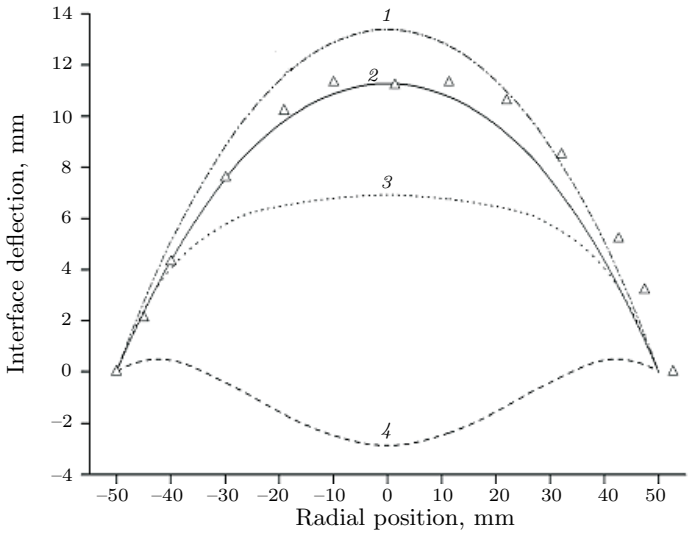


*Fig. 3.* Comparisons of the interfacial deflection in the experimental data [21] with the results by the present simulations of turbulence models. Relative error: $10^{-4}$, mesh number: 8685, crystal height: 300 mm, crystal diameter: 100 mm. *1* – one equation model, *2* – Chien $k$-$\epsilon$ model, *3* – Spalart-Almaras model, *4* – standard $k$-$\epsilon$ model, △ - experimental data [21]. The results of Chien $k$-$\epsilon$ model approach most closely the experimental data.

**4. Results and discussion.** Before conducting the simulations, tests of grid convergences are performed. At the stage of global calculations, three different meshes are implemented. It has been found that the results for a gird number of 35708 nodes agree quite well with a finer mesh of 51195 nodes. As a result, the grid of global domain consisting of 35708 nodes is applied, and its typical temperature distribution is shown in Fig. 2*a*. These simulated results are thus taken as the boundary conditions to the Flow Module simulations. For the Flow Module simulations, we have tested grids consisting of 7355, 12235 and 35740 nodes. They all converge quite well in terms of the interfacial deflections, so that the intermediate number of 12235 nodes is chosen for the further calculations. The temperature distribution of a representative Flow Module simulation without influences from a magnetic field is demonstrated in Fig. 2*b*. In order to focus on the flow fields and temperature distributions of the melt as well as on the shape of the crystal interface, only the region in the crucible, which contains the silicon melt, is demonstrated in the following discussion.

*4.1. Effects of a cusp field on flow fields and temperature distributions of the melt.* We first investigate the effects of the magnetic field for the case of $dy = 0$, in which the coils' center is located right at the interface. The comparisons of the melt flow patterns and temperature distributions in the crucible between field strengths of $B = 0$ and $B = 0.05\,\mathrm{T}$ are shown in Fig. 4. Without applying a cusp field, as shown in Fig. 4*a*, it is clear that three separate vortexes exist in the melt. In the core region right under the crystallization front, a fast downward motion of the melt is driven by natural convection. In contrast, the melt flow velocity is slower in the outer part of the crucible. On the other hand, even the downward motion of the melt flow under the crystallization front can still be

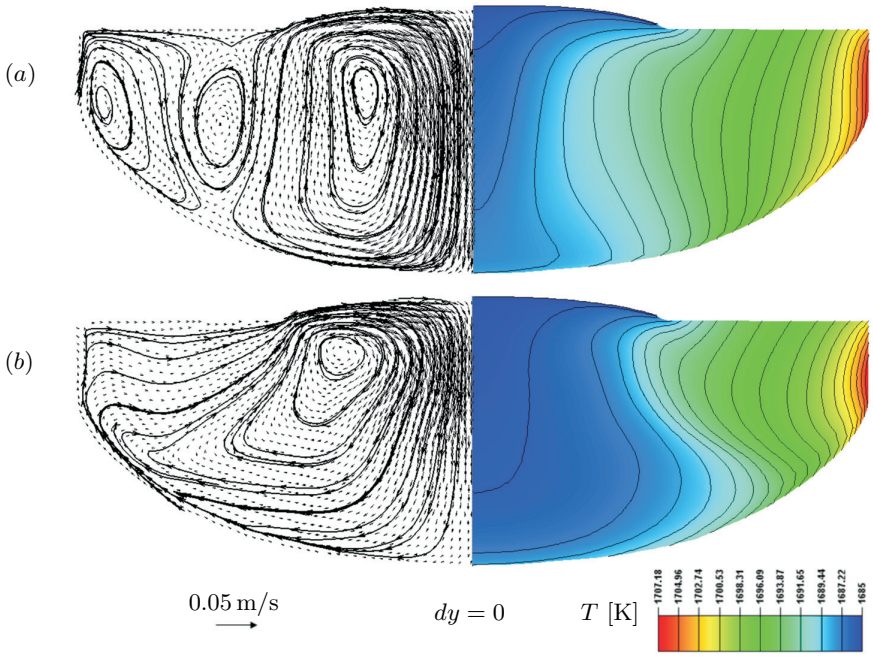


*Fig. 4.* Melt flow patterns (left) and temperature distributions (right) inside the crucible (*a*) without a cusp field, and (*b*) with a cusp magnetic field of $B = 0.05\,\mathrm{T}$. The presence of the magnetic field leads to more stable flow patterns, and thus weakens natural convection.

observed under the influences of a cusp field shown in Fig. 4*b*; the motion is slower due to the weakened natural convection by the Lorentz forces. Therein, only one vortex is formed in the melt under the cusp field condition. The suppression of the vortexes can be explained by the orientation of the magnetic field. The cusp field generates a magnetic flux, whose orientation is opposite to the main local convective vortexes, i.e. counter-clockwise in the left half part of the melt and vise versa. As a result, the strengths of the local vortexes are weakened. It should be noted that the velocity suppression can also reduce particles generated by crucible corrosion, and thus decreases the probability of dislocation [13]. As to the temperature distributions, the lower temperature region, which is located mainly in the inner area under the solidified crystal, is enlarged due to the cusp field. In addition, the temperature variation along the horizontal direction is obviously more significant with the presence of the cusp field. The area of lower temperature extends to approach the outer region of the crucible. These changes are the consequences of the local magnetic flux, whose orientation is clockwise in the right half part of the melt as mentioned above. The Lorentz forces induced by the magnetic flux push the isothermal contours horizontally away from the central axis, so that the temperature variation appears more prominent near the vertical side of the crucible. The overall pattern of the isothermal contour lines appears more curving in the presence of the close-loop magnetic flux rather than nearly vertical without the cusp field. The larger lower temperature region under the crystal and a more significant horizontal temperature variation are responsible for the less intensive natural convention in the cusp field situation.

*4.2. Influences for different locations of the magnet coils.* Figs. 5 and 6 show the flow fields and the corresponding temperature profiles of the melt in the

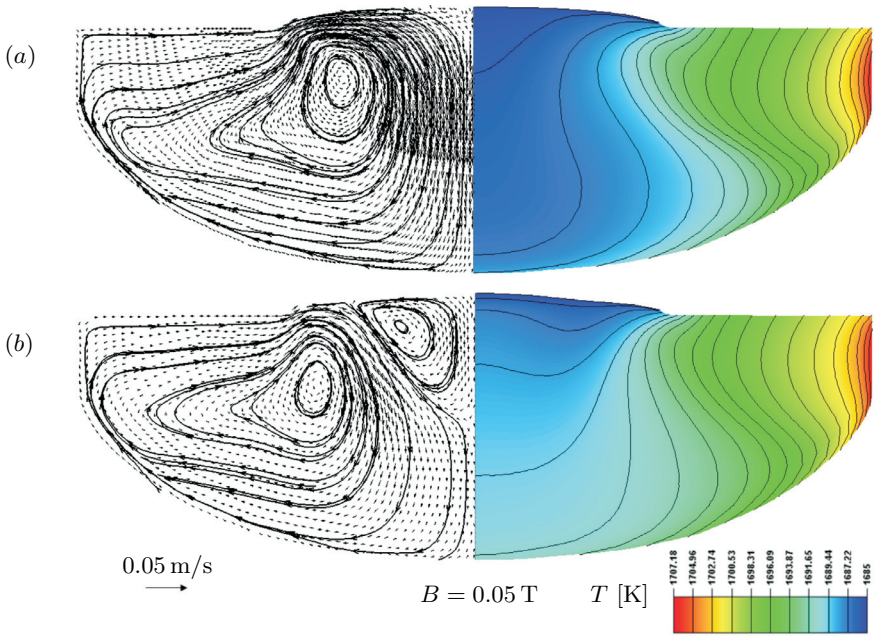


*Fig. 5.* Melt flow patterns (left) and temperature distributions (right) inside the crucible for higher positions of the magnet coils at (*a*) $dy = 5$ cm and (*b*) $dy = 10$ cm. The downward melt velocity right under the solidified crystal is suppressed more effectively for a larger value of $dy$. The counter-rotating secondary vortex is observed for case of $dy = 10$ cm.

crucible for the cases of $dy = \pm 5$ and $\pm 10$ cm, respectively, under a cusp field of $B = 0.05$ T. These figures can be compared with the case of $dy = 0$ shown in Fig. 4b to identify the effects of the coils' position. Since the horizontal zero-flux axis lies above the melt surface for a positive dy, the local effects of the magnetic flux in the vertical direction, which acts upwards under the present condition, are enhanced. As a result, the vertical melt velocity in the core region right under the crystal is reduced more significantly if the coils' center is further away from the interface. Fig. 5*a* clearly demonstrates a large vortex with a milder downward motion near the center in the crucible for cases of $dy = 5$ cm. The enhancement of induced upward magnetic effects would completely suppress the convective vortex for $dy = 10$ cm, and a more unstable flow pattern with a secondary counter rotating vortex is generated as shown in Fig. 5*b*. For corresponding temperature profiles compared with the case of $dy = 0$ cm in Fig. 4*b*, it is evident that more isothermal contour-lines distribute horizontally at the central region for a larger height of $dy$. In the case of $dy = 10$ cm, these isothermal lines are almost evenly distributed at the central region. This fact confirms a stronger upward magnetic effect. The reduced vertical velocity leads to a less natural convection, which is favorable to the process of crystal growth. On the other hand, the more unstable flow pattern, such as in the case of $dy = 10$ cm, might affect the shape of the interface. As a result, the influences of the positive height of coils' positions appear more complex, and a careful evaluation for an optimal position of the coils is essential.

We now discuss the cases of negative $dy = -5$ and $-10$ cm as shown in Fig. 6. Because the location of the zero-flux axis is now placed lower than the crystal surface, the melt region would be affected by two counter-directed magnetic fluxes. For the region below the zero-flux axis, a similar upward effect near the center is induced as mentioned in the previous paragraph. Nevertheless, the magnetic

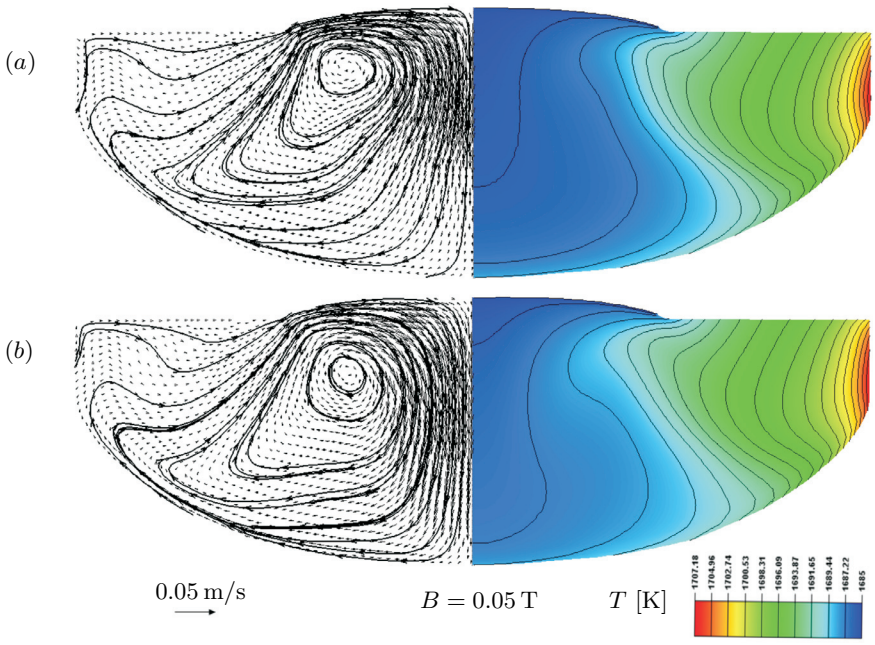


*Fig. 6.* Melt flow patterns (left) and temperature distributions (right) inside the crucible for lower positions of the magnet coils at (*a*) $dy = -5$ cm and (*b*) $dy = -10$ cm. Overall patterns of the velocity and temperature fields are similar to the case of zero $dy$.

flux induces a motion downwards in the region above the zero-flux axis due to another magnetic flux loop. As a result, strengths of local upward flows are not suppressed as significantly as for the cases of positive $dy$. On the other hand, the outward magnetic influences are enhanced horizontally near the surface because of the presence of an additional flux loop. The counter-effects of weaker vertically upward suppression near the center and a stronger horizontally outward stretch near the surface lead to the overall patterns of velocity and temperature fields similar to the case of zero $dy$.

*4.3. Corresponding interface deflection and the $V/G$ parameter.* The profiles of the interface deflection for the cases of $dy = 0$, 5, 10, $-5$, and $-10$ cm under the influence of a cusp field of $B = 0.05$ T are displayed in Fig. 7*a*. In general, a flatter interface is desired. A smaller interface deflection value can diminish the

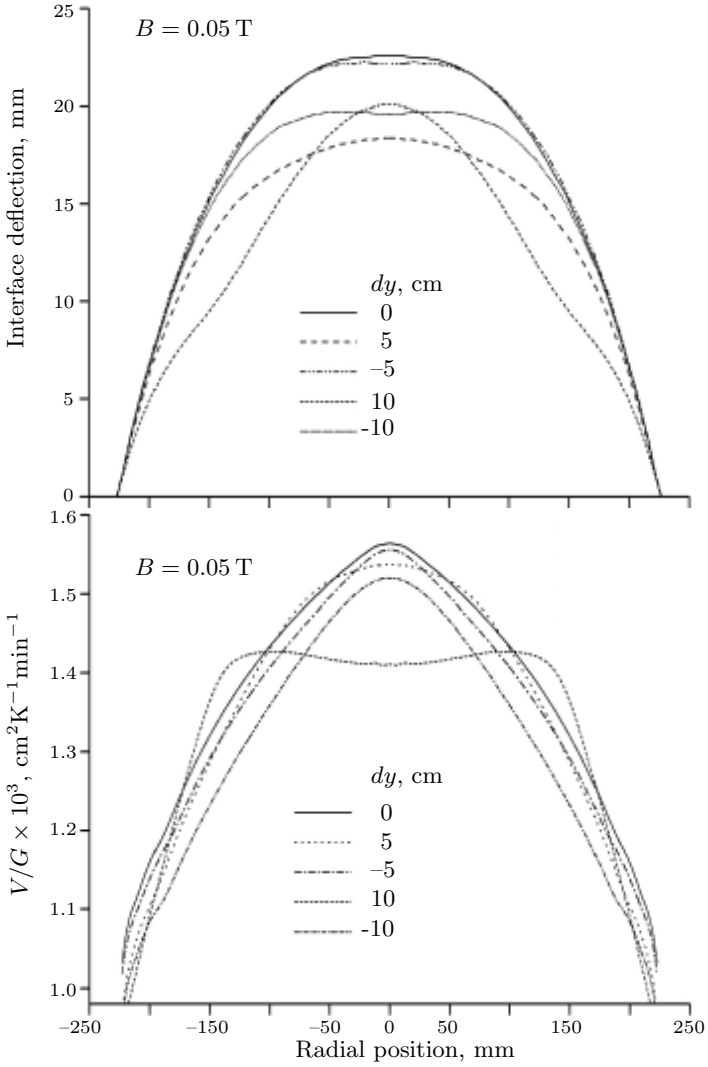


*Fig. 7.* (*a*) Deflections of the crystallization front, and (*b*) distributions of the $V/G$ parameter along the melt and crystal interface. Determined by less interfacial deflections and a critical $V/G$ value of $1.5 \cdot 10^{-3}$ cm$^2$K$^{-1}$min$^{-1}$, an intermediate value of positive $dy = 5$ cm is desired.

probability of dislocation. It is worth noting that the case of $dy = 0$ has the largest deflection value, and this value can be improved by adjusting the positions of the magnet coils. It is clear that the case of $dy = 5\,\text{cm}$ has a smaller interface deflection. This is consistent with the findings of velocity and temperature fields presented previously, in which the natural convective vortex is effectively suppressed without forming an additional secondary vortex. The variation of the interface shape for the case of $dy = 10\,\text{cm}$ is sharper because of generation of the secondary vortex. The interfaces appear as slightly saddle shapes for $dy = -5$ and $-10\,\text{cm}$ due to the combined effects of weaker vertically upward constraints associated with a stronger horizontal outward stretch. A critical ratio of the crystal pulling rate over the temperature gradient in the crystal (often denoted as the $V/G$ parameter), which is $1.5 \cdot 10^{-3}\,\text{cm}^2\text{K}^{-1}\text{min}^{-1}$ or slightly higher than this value, is commonly used as a simplified criterion of growing silicon crystals for a low concentration of self-vacancies [22, 23]. As demonstrated in Fig. 7*b*, except for the case of $dy = 10\,\text{cm}$ when the flow field is more unstable due to the presence of a secondary vortex, all cases with non-vanish $dy$ have better $V/G$ values than the case of zero $dy$. The results of Figs. 7*a*, *b* clearly show that the profiles of the interface deflection and the $V/G$ value in the silicon crystal growth are highly sensitive to the positions of the magnet coils. The $V/G$ distributions for $dy = 0$, $\pm 5$, and $-10\,\text{cm}$ cases are quite close to the optimal value of $V/G$. The results of the interface inflection for the cases of $dy = 0$, $-5$, and $-10\,\text{cm}$ do not look promising for the production of perfect crystals because their degrees of deflection are larger than the case of $dy = 5$. As a result, this study suggests that placing the coils' center at an intermediate position higher than the crystal interface would result in an optimal growth of silicon crystals.

**5. Conclusions.** In this work, the effects of various magnet coils' positions on the melt flow patterns and temperature distributions for the Si CZ crystal growth subjected to a fixed cusp magnet field have been successfully simulated by means of a commercially available CGsim software package. The corresponding interface deflection and the $V/G$ parameter are investigated as well to determine the optimal process. The simulation is first validated by comparing the published experimental data in a field free condition. If the central horizontal axis is place right at the interface, the configuration of the cusp field generates close-loop magnetic fluxes of counter-rotating orientation to the natural convective vortexes. Generally, the presence of the magnetic field stabilizes flow patterns of the melt in terms of reducing both the number and the strengths of the vortexes induced by natural convection, which is favorable to the growth. Further improvements can be obtained by varying the distances, denoted as $dy$, of the magnet coils away from the melt interface. With a positive dy, whose center of the field is placed above the melt interface, the natural convection right beneath the solidified crystal is suppressed more effectively. As a result, the deflection of the interface is improved. Nevertheless, with an excessive large value of $dy$, a too strong local magnetic effect might lead to the formation of a counter-rotating secondary vortex near the central region of the melt. The formation of this secondary vortex causes a sharper interface. On the other hand, with negative values of $dy$, the magnetic effects are more complicated, in which the convective downward motion is less suppressed associated with a stronger constraint in the horizontal inward motion. Considering the overall factors of desired interfacial profiles and the critical $V/G$ parameter, it is suggested that an intermediate value of positive dy is desired for producing crystals of better quality.

## REFERENCES


[1] Y. Shiraishi, K. Takano, J. Matsubara, T. Iida, N. Takase, N. Machida, M. Kuramoto, H. Yamagishi. *J. Crystal Growth*, **229** (2001), p. 17.

[2] L. Gorbunov, A. Klyukin, A. Pedchenko, A. Fedorov. *Energy Convers. Manage*, **43** (2002), p. 317.

[3] B. Nacke, H. Kasjanow, A. Krause, A. Muižnieks, F.-M. Kiessling, U. Rehse, P. Rudolph. *Magnetohydrodynamics*, **45** (2009), p. 317.

[4] O. Gräbner, A. Mühe, G. Müller, E. Tomzig, J. Virbulis, W.V. Ammon. *Mater. Sci. Eng.*, **B73** (2000), p. 130.

[5] A. Cramer, M. Röder, J. Pal and G. Gerbeth. *Magnetohydrodynamics*, **46** (2010), p. 353.

[6] I.Ch. Avetissov, A.P. Sadovskii, E.A. Sukhanova, E.V. Zharikov, A.I. Belogorokhov, B.N. Levonovich. *J. Crystal Growth*, **312** (2010), p. 1104.

[7] A. Krauze, N. Jēkabsons, A. Muižnieks, A. Sabanskis, U. Lācis. *J. Crystal Growth*, **312** (2010), p. 3225.

[8] M.H. Tavakoli, H. Karbaschi, F. Samavat, E. Mohammadi-Manesh. *J. Crystal Growth*, **312** (2010), p. 3198.

[9] O. Klein, C. Lechner, P.E. Druet, P. Philip, J. Sprekels, C. Frank-Rotsch, F.M. Kiessling, W. Miller, U. Rehse, P. Rudolph. *Magnetohydrodynamics*, **45** (2009), p. 557.

[10] A. Krauze, A. Rudevičs, A. Muižnieks, A. Sabanskis, N. Jēkabsons, B. Nacke. *Magnetohydrodynamics*, **45** (2009), p. 605.

[11] O. Klein, C. Lechner, P.É. Druet, P. Philip, J. Sprekels, C. Frank-Rotsch, F.M. Kiessling, W. Miller, U. Rehse, P. Rudolph. *J. Crystal Growth*, **310** (2008), p. 1523.

[12] P. Rudolph. *J. Crystal Growth*, **310** (2008), p. 1298.

[13] C. Lechner, O. Klein, P.É. Druet. *J. Crystal Growth*, **303** (2008), p. 161.

[14] V.V. Kalaev. *J. Crystal Growth*, **303** (2007), p. 203.

[15] Y. Kishida, T. Tamaji, K. Okazawa, W. Ohashi. *J. Crystal Growth*, **273** (2005), p. 329.

[16] T. Munakata, S. Someya, I. Tanasawa. *Int. J. Heat Mass Trans.*, **47** (2004), p. 4525.

[17] Y. Shiraishi, S. Maeda, K. Nakanura. *J. Crystal Growth*, **266** (2004), p. 28.

[18] A. Krauze, A. Muiznieks, A. Mühlbauer, T. Wetzel, L. Gorbunov, A. Pedchenko, J. Virbulis. *J. Crystal Growth*, **266** (2004), p. 40.

[19] N.G. Ivanov, A.B. Korsakov, E.M. Smirnov, K.V. Khodosevitch, V.V. Kalaev, Y.N. Makarov, E. Dornberger, J. Virbulis, W.V. Ammon. *J. Crystal Growth*, **250** (2003), p. 183.

[20] D. Vizman, O. Gräbner, G. Müller. *J. Crystal Growth*, **236** (2002), p. 545.

[21] D.P. Lukanin, V.V. Kalaev, Y.N. Makarov, T. Wetzel, J. Virbulis, W.V. Ammon. *J. Crystal Growth*, **266** (2004), p. 20.

[22] Flow Module. *Theory Manual, Version 9.02* (Semiconductor Technology Research, Inc., Richmond, VA, September 2006).

[23] R.A. Brown, Z. Wang, T. Mori. *J. Crystal Growth*, **225** (2001), p. 97.

[24] M. Kulkarni. *Ind. Eng. Chem. Res*, **44** (2005), p. 6246.

Received 22.03.2011